
BREATHER BOUND STATES IN A PARAMETRICALLY DRIVEN MAGNETIC WIRE

A PREPRINT

✉ **Camilo José Castro**^{*1,2}, **Ignacio Ortega-Piwonka**³, **Boris A. Malomed**⁴, **Deterlino Urzagasti**², **Liliana Pedraja-Rejas**⁵, **Pablo Díaz**⁶, and **David Laroze**^{†1}

¹Instituto de Alta Investigación, Universidad de Tarapacá Casilla 7D, Arica 1000000, Chile

²Carrera de Física, Universidad Mayor de San Andrés, La Paz, Bolivia

³Grupo de Dinámica No Lineal, Caos y Sistemas Complejos, Universidad Rey Juan Carlos, Tulipán s/n, Móstoles 28933, Spain

⁴Department of Physical Electronics, School of Electrical Engineering, Faculty of Engineering, and Center for Light-Matter Interaction, Tel Aviv University, Tel Aviv 69978, Israel

⁵Departamento de Ingeniería Industrial y de Sistemas, Universidad de Tarapacá, Casilla 7D, Arica 1000000, Chile

⁶Departamento de Ciencias Físicas, Universidad de La Frontera, Casilla 54-D, Temuco, Chile

November 22, 2024

ABSTRACT

We report the results of systematic investigation of localized dynamical states in the model of a one-dimensional magnetic wire, which is based on the Landau-Lifshitz-Gilbert (LLG) equation. The dissipative term in the LLG equation is compensated by the parametric drive imposed by the external AC magnetic field, which is uniformly applied perpendicular to the rectilinear wire. The existence and stability of the localized states is studied in the plane of the relevant control parameters, *viz.*, the amplitude of the driving term and the detuning of its frequency from the parametric resonance. With the help of systematically performed simulations of the LLG equation, existence and stability areas are identified in the parameter plane for several species of the localized states: stationary single- and two-soliton modes, single and double breathers, drifting double breathers with spontaneously broken inner symmetry, and multi-soliton complexes. Multistability occurs in this system. The breathers emit radiation waves (which explains their drift caused by the spontaneous symmetry breaking, as it breaks the balance between the recoil from the waves emitted to left and right), while the multi-soliton complexes exhibit cycles of periodic transitions between three-, five-, and seven-soliton configurations. Dynamical characteristics of the localized states are systematically calculated too. These include, in particular, the average velocity of the asymmetric drifting modes, and the largest Lyapunov exponent, whose negative and positive values imply that the intrinsic dynamics of the respective modes is regular or chaotic, respectively.

Keywords Landau-Lifshitz equation · dispersive radiation · soliton dynamics; Lyapunov exponents · multistability

1 Introduction

Pattern formation in nonlinear dissipative media relies on the coexistence of two balance conditions: between the nonlinear self-focusing and linear self-stretching, under the action of diffraction and/or dispersion, and between dissipative losses and a compensating mechanism. In physical systems governed by complex Ginzburg-Landau equations, the losses are balanced by the intrinsic gain Aranson and Kramer [2002], Rosanov [2013], while in passively driven optical cavities the compensation is provided by an external pump, as modeled by the Lugiato-Lefever equation Lugiato and Lefever [1987], Kartashov et al. [2017].

*ccastro@fiumsa.edu.bo

†dlarozen@academicos.uta.cl

The parametrically-driven damped nonlinear Schrödinger (PDNLS) equation Miles [1984], Barashenkov et al. [1991] is known as a universal model of periodically forced dissipative systems. Solutions of this equation are known to produce various dynamical regimes, including stationary, periodic, and chaotic ones, such as Faraday waves Faraday [1831], Scott [1969], Couillet et al. [1994], Clerc et al. [2010a], single solitons Barashenkov et al. [1991, 2011], Alexeeva et al. [2000], Barashenkov and Zemlyanaya [1999], Zemlyanaya and Alexeeva [2009], two-soliton states Barashenkov and Zemlyanaya [2011], Urzagasti et al. [2012], as well as spatiotemporal chaos Barashenkov et al. [1991], Shchesnovich and Barashenkov [2002]. The parametric instability of a vertically vibrated Newtonian fluid, modeled by the PDNLS equation, leads to notable hydrodynamic phenomena manifested by standing (Faraday) waves on its surface Faraday [1831]. These standing waves are most sensitive to the parametric forcing at half its frequency (the 2 : 1 parametric resonance) Arnold [2012]. In weakly dissipative systems, the PDNLS equation captures the development of the parametric instability occurring near the 2 : 1 resonance Clerc et al. [2009a]. In this context, it is relevant to mention that stabilization of dissipative solitons by the parametric drive was studied in various contexts, such as the periodically time-modulated damped nonlinear Schrödinger equation for wave amplitudes Okamura and Konno [1989], Barashenkov et al. [1991], and chains of coupled pendula Denardo et al. [1992], just to mention a few. Chaotic dynamical states generated by the PDNLS equation have been studied in detail too Bondila et al. [1995], Barashenkov and Smirnov [1996]. Also investigated were bound states of solitons in the same model, chimeras and localized dynamical chaos in parametrically-driven nonlinear lattices in the discrete version of the equation Cabanas et al. [2021a], as well as periodic waves and multistable dissipative solitons produced by the parametrically-driven version of the complex Ginzburg-Landau equation (in other words, the PDNLS equation with complex coefficients in front of the dispersion and nonlinearity terms) Barashenkov et al. [2003], Sakaguchi and Malomed [2003]. Patterns and localized structures produced by (generalized) PDNLS and related equations can be found in Refs. Reyes et al. [2024], León et al. [2015], Leon et al. [2024], Moille et al. [2024], Bogdan and Charkina [2022], Shaukat et al. [2022], Cabanas et al. [2021b], Urzagasti et al. [2017, 2014a], Marín et al. [2023], Barbosa et al. [2023], Dileep and Murugesu [2023], Parra-Rivas et al. [2022], Englebert et al. [2021], Diamantidis et al. [2021], Yamaguchi and Hourii [2021], Mertens and Quintero [2020], Barashenkov and Chernyavsky [2020], Urra et al. [2019], Edri et al. [2020], Ferré et al. [2017], Clerc et al. [2014].

Among various physical settings, nonlinear phenomena are common in magnetic materials. In the classical regime, the appropriate model for the magnetization dynamics is provided by the Landau-Lifshitz-Gilbert (LLG) equation Bertotti et al. [2009] and its generalizations Scholz and Batra [2008], Lakshmanan [2011]. In the case of magnetic nanoparticles, where magnetization is represented by a single magnetic domain, both theoretical and experimental studies have explored different routes to periodicity, chaos, and multistability Montoya et al. [2019], Bragard et al. [2021], Alvarez et al. [2000], Perez et al. [2015], Smith et al. [2010], Leon et al. [2024], Vélez et al. [2020], Feron and Camley [2017], Smith et al. [2009], Sementsov [2009], Botha et al. [2023], Shen and Shen [2024], Yamaguchi et al. [2023]. A relevant possibility is to include additional terms in the equation that account for magnetic inertia Unnikandanunni et al. [2022], Rodriguez et al. [2024]. In the case of objects where spatial dimensions play a fundamental role, such as wires (both straight and curved ones), tubes, membranes, cubes, tori, etc., a wide variety of magnetic textures and a broad range of pattern-formation regimes have been discovered. Among them, well-known examples are vortices, skyrmions, and droplets Jain et al. [2012], Pivano and Dolocan [2016], Guslienko et al. [2010], Ovcharov et al. [2024], d’Aquino et al. [2023], Gareeva and Guslienko [2023], Fert et al. [2017], Jiang et al. [2024], Garcia-Sanchez et al. [2016], Jiang et al. [2017], Deng et al. [2022], Kosevich et al. [1990], Mohseni et al. [2013], Roessli et al. [2001], Rothos et al. [2023].

Two classes of physically relevant states in dissipative magnetic media, where losses can be counterbalanced by the parametric drive in the form of a periodically time-modulated (AC) external magnetic field, are magnetic solitons and Faraday waves. In this scenario, the parametrically-driven LLG equation near the 2 : 1 parametric resonance can be approximated by the PDNLS equation Barashenkov et al. [1991]. Therefore, all the phenomena predicted by the PDNLS equation can be also observed in the framework of its LLG counterpart. In particular, standing waves, pulses, solitons, breathers, and the interaction of in-phase and out-of-phase stationary solitons in magnetic wires, as well as solitons and magnetic textures in the magnetic plane, have been studied in this parametrically driven context Clerc et al. [2010a, 2008, 2009b,a, 2010b], Urzagasti et al. [2013]. However, the previous studies of PDNLS-based models did not address the complexity of non-stationary *bound states of solitons*, which is an essential direction for the extension of the work on this topic.

This work aims to tackle this possibility, addressing novel dynamical scenarios involving the interaction of two one-dimensional solitons in a parametrically driven magnetic chain, treated in the continuum approximation. Starting from the parametrically-driven LLG model, we demonstrate that the interacting solitons either merge into a single mode or form a clearly identified bound state. Previously unexplored complex dynamical states emerge as an extension of the basic soliton dynamics. Specifically, by varying the model parameters, we observe that standing waves exhibit an oscillatory instability. Further changes in the parameters lead to a secondary oscillatory instability, which gives rise to spontaneous symmetry breaking of double breathers, which is accompanied by their drift, and, eventually,

spatiotemporal chaos. The dynamics are quantified by dint of several indicators, including bifurcation diagrams and Lyapunov exponents.

The manuscript is structured as follows: Sections 2 and 3 present, respectively, the model and scheme of the adopted numerical analysis. Dynamical indicators, used for the characterization of various novel states produced by the model, are introduced in Section 4. Systematic numerical results and the corresponding discussion are reported in Section 5, and the paper is concluded by Section 6.

2 The theoretical model

We consider a magnetic wire, with the normalized magnetization field $\mathbf{m} = \mathbf{m}(\mathbf{r}, t)$, where \mathbf{r} and t represent the spatial coordinates and time, respectively. We concentrate on a ferromagnetic anisotropic long wire, assuming that the propagation of magnetization waves along the wire axis, i.e., in the direction represented by $\hat{\mathbf{z}} = (0, 0, 1)$ Aharoni [2001], is governed by the LLG equation. In particular, this equation was used to model a one-dimensional magnetic wire driven by a time-modulated magnetic field applied in the perpendicular direction, to study the transition from regular solitons to regular bound states Urzagasti et al. [2012]. Here we employ the same setup, as shown in Fig. 1(a). For this setting, the LLG equation can be cast in the form of

$$\frac{\partial \mathbf{m}}{\partial t} = -\mathbf{m} \times \mathbf{\Gamma} + \alpha \mathbf{m} \times \frac{\partial \mathbf{m}}{\partial t}. \quad (1)$$

where $\mathbf{\Gamma}$ is the effective torque and α is the damping coefficient. This equation is derived from the general LLG model by taking into regard that the scaled magnetization vector, \mathbf{m} , which represents the local orientation of constituent particles of the medium, keeps a constant absolute value, $|\mathbf{m}|^2 = 1$ and assuming the one-dimensional evolution of the \mathbf{m} field along coordinate z . In this case, the effective torque in Eq. (1), acting upon the magnetization in a long wire, may be approximated as

$$\mathbf{\Gamma} = \frac{\partial^2 \mathbf{m}}{\partial z^2} - \beta(\mathbf{m} \cdot \hat{\mathbf{z}})\hat{\mathbf{z}} + \mathbf{h}. \quad (2)$$

It includes scaled parameter β accounting for the anisotropy along the z -axis, which depends on properties of the magnetic medium, and the external modulated magnetic field composed of constant (DC) and time-modulated (AC) terms, *viz.*,

$$\mathbf{h}(t) = (h_c + h_0 \cos(\Omega t))\hat{\mathbf{x}}, \quad (3)$$

where h_c , h_0 , Ω , and $\hat{\mathbf{x}}$ are the modulation offset, AC amplitude, frequency, and the unit vector perpendicular to the wire, respectively Urzagasti et al. [2012].

In the application to a single magnetic particle, which does not admit spatial dependence, the LLG equation exhibits a variety of stable equilibrium solutions, including the fixed attractor with $\mathbf{m} = \hat{\mathbf{x}}$, when the modulation is null (i.e., $h_0 = 0$). This means that the magnetization is aligned to the DC magnetic field. When the AC field is present, one can find periodic, quasi-periodic, and chaotic responses Laroze et al. [2011, 2012]. In particular, small perturbations around the stationary attractor produce damped oscillations with frequency $\Omega_0 = \sqrt{h_c(h_c + \beta)}$. The attractor becomes unstable via an oscillatory instability when the magnetic field is modulated with a frequency close to the parametric-resonance value,

$$\Omega = 2(\Omega_0 + \nu), \quad (4)$$

where ν is the detuning from the resonance. Specifically, this bifurcation occurs when the modulation amplitude surpasses a critical value related to ν by the following equation:

$$(h_0^{\text{crit}})^2 = \left(\frac{4\Omega_0}{\beta}\right)^2 \left(\nu^2 + \left(\frac{\alpha(\beta + 2h_c)}{2}\right)^2\right). \quad (5)$$

Under this condition, the magnetic particle responds by subharmonic oscillations along the x and y -axis, directly exhibiting the parametric resonance Clerc et al. [2010b]. Equation (5) corresponds to a hyperbola in the (ν, h_0) plane, which represents the first Arnold tongue in the system.

When the spatial coupling is incorporated into the model, the system exhibits a rich variety of responses including the uniform state, $\mathbf{m}(z, t) = \hat{\mathbf{x}}$, inside the Arnold tongue, subharmonic patterns predominantly located over the tongue, as well as domain walls, single solitons, and double solitons. A comprehensive summary of the single-soliton regime, which arises right under the Arnold tongue, is displayed in Ref. Urzagasti et al. [2013]. For small values of the modulation drive h_0 , the soliton shows the usual behavior with subharmonic oscillations. However, for higher values of the drive, starting from $h_0 \approx 0.44$, the solitons exhibit features typical for breathers Kibler et al. [2022], such as

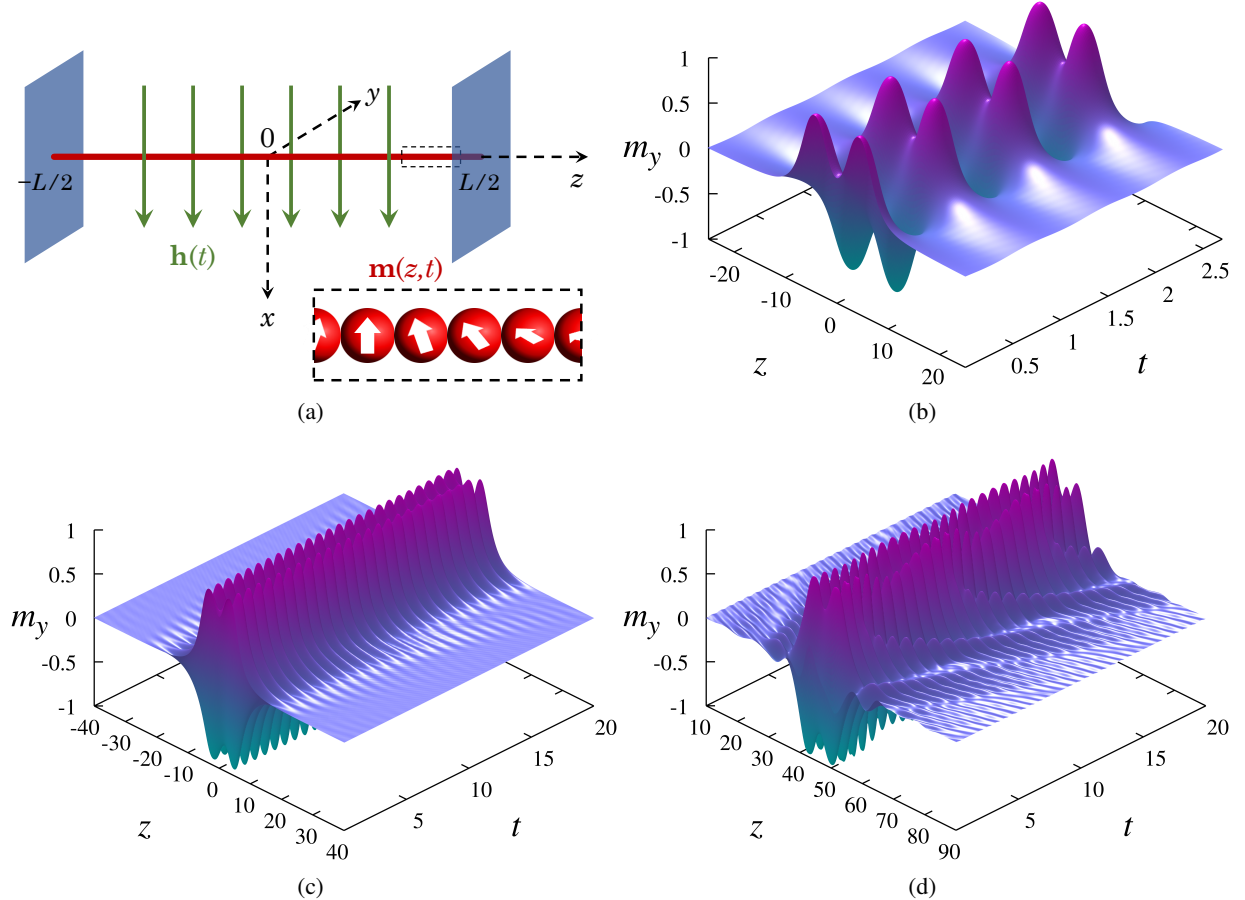


Figure 1: (color online) **(a)** The schematic of the one-dimensional wire aligned with the z -axis. The wire is made of magnetic particles subjected to the action of the perpendicular time-modulated magnetic field, $\mathbf{h}(t)$. As a result, the magnetization of the constituent particles (schematically denoted by white arrows in the inset), which is represented by continuous field $\mathbf{m}(z, t)$, is polarized according to LLG equation (1). **(b–d)** Simulations of Eq. (1) showing the double-soliton response for different values of the modulation parameters, namely: **(b)** $(\nu, h_0) = (-0.3, 0.55)$ (the standard double soliton); **(c)** $(\nu, h_0) = (-0.44, 0.65)$ (a symmetric breathing double soliton); **(d)** $(\nu, h_0) = (-0.402, 0.636)$ (an asymmetric breathing double soliton).

the emission of low-amplitude dispersive waves and the oscillation amplitude that varies on a long timescale. The distinction between the standard and breather solitons in the space of parameters is revealed by the numerical analysis based on the fast-Fourier-transform algorithm. It identifies a well-defined boundary between these dynamical regimes, without any coexistence region Urzagasti et al. [2013].

Following the pattern of Ref. Urzagasti et al. [2012], we here intend to perform the analysis of the double-soliton response for different values of the modulation parameters in Eqs. (3) and (4), scanning the (ν, h_0) plane. The other parameters are fixed as in Ref. Urzagasti et al. [2012], *viz.*, $\alpha = 0.0015$, $\beta = 20$ and $h_c = 3$, and the wire's length is chosen as $2L = 250$ (these are values relevant to the respective experimental setup). As shown in Fig. 1, the double solitons may exhibit either the usual (panel (b)) or breathing (panels (c,d)) behavior, depending of the values of ν and h_0 . Similar to single-breather states, double breathing solitons emit dispersive waves. In some cases (panels (b) and (c)), amplitudes of the bound solitons remain identical in the course of the long evolution, *i.e.*, the response exhibits symmetry with respect to the midpoint between the solitons. However, in other cases (panel (d)), the symmetry is spontaneously broken, and the amplitudes of the bound solitons may differ significantly. The asymmetric double breathers also exhibit a slow steady drift, not found in the other single- and double-soliton regimes, on top of random fluctuations of their positions. Naturally, the one-sided drift of the breather is made possible by its spontaneously emerging asymmetry.

3 The numerical framework

We simulated Eq. (1) by means of FORTRAN 90, using the fifth-order, double-precision, variable-step Runge-Kutta method, with monitoring of the local truncation error Press et al. [1993]. Equation (1) is supplemented by the Neumann's boundary conditions imposed at edges of the integration domain, *viz.*, $\partial \mathbf{m} / \partial z = 0$ at $z = \pm L$. The accuracy or tolerance level was adopted at the level of $10^{-5}\%$. The spatial discretization was implemented with $dz = 1/6 \approx 0.17$, in the domain of size $-125 < z < +125$. The accuracy of the numerical scheme was earlier established in Ref. Urzagasti et al. [2014b, 2013]. The simulations were run for different values of parameters (ν, h_0) in Eqs. (3) and (4), with ν and h_0 ranging from -0.7 to 0 , and from 0.3 to 0.9 , respectively. For both these parameters, the variation step was 0.002 , except inside the region of the standard single soliton, where the step was 0.01 (five times coarser), as dynamical indicators of this regime are well known Urzagasti et al. [2014b, 2013]. The simulations were run in parallel using MPI FORTRAN. To assess the reproducibility of the model and the reliability of the algorithm, simulations were also run using Python 3.11, accelerated with Numba 0.56.

The initial conditions were set symmetrically with respect to $z = 0$, approximately corresponding to two solitons separated by distance $\Delta z = 7$, while keeping the unitary field magnitude ($|\mathbf{m}| \equiv 1$) everywhere along the wire:

$$\begin{aligned} m_y(z, t = 0) &= \frac{1}{2} (\operatorname{sech}(z + 3.5) + \operatorname{sech}(z - 3.5)), \\ m_z(z, t = 0) &= 0.95 m_y, \\ m_x(z, t = 0) &= \sqrt{1 - m_y^2 - m_z^2}. \end{aligned} \quad (6)$$

The timeline of each simulation was divided into three different stages. The first one is the transient stage, when the system starts its evolution from input (6). The sampling timestep adopted for this stage was $dt = 5^3/2^6 \approx 1.95$, and its duration was $\Delta t = 5 \times 10^3 \approx 2560 \times dt$, after which we can safely assume that the system has reached a steady state. During the next, steady-state, stage a number of dynamical indicators were computed to gather relevant information about the system, including its response type. This stage had duration $\Delta t = 10^3$, while the sampling timestep was adopted as $dt = 5^3/2^{14} \approx 0.0076 \approx \Delta t/131600$, being much shorter than the modulation period of the AC magnetic field, see Eq. (3). Data for the computation of the largest Lyapunov exponent (LLE) for the dynamical regimes were collected in the course of the longer third stage, with duration $\Delta t = 14 \times 10^3$ and sampling time step $dt = 5^3/2^7 \approx 0.98 \approx \Delta/14300$.

4 Dynamical indicators

Addressing the last part of the transient stage of the simulations, *viz.*, $t \in [4000, 5000]$, spatially uniform solutions and fast-moving localized modes were excluded from the analysis. Those states are irrelevant for the present work, as they are not related to the single- and double-soliton regimes, which are the target of the consideration. To distinguish the irrelevant states from the relevant ones, the coordinate of the center of mass (CM) of the soliton (or solitons) potentially appearing in the magnetization field was calculated as

$$z_{\text{CM}}(t) = \frac{\int_{-L}^{+L} z \cdot m_y^2(z, t) dz}{\int_{-L}^{+L} m_y^2(z, t) dz}. \quad (7)$$

We focused on the m_y component of the magnetization field, as $m_y = 0$ in the uniform state, while solitons give rise to a local excitation of m_y . The CM mean velocity of the drifting solitons was found by fitting the time series $z_{\text{cm}}(t)$ to a linear dependence, and taking its slope. Modes with the drift velocity exceeding 0.005 are considered as fast-moving ones and dismissed from the subsequent analysis due to artifacts expected from their collisions with the boundaries of the simulation box. This problem will be eliminated if a ring-shaped wire is considered, with periodic boundary conditions, which will be the subject of a separate work.

Additionally, the following integral characteristic was computed,

$$I_D = \int_{4000}^{5000} \left[\frac{1}{2L} \int_{-L}^{+L} (m_y(z, t))^2 dz \right]^2 dt. \quad (8)$$

It provides a measure of the departure of the given state from the uniform one, which has $I_D \equiv 0$. Subsequently, I_D can be used to roughly estimate what share of the entire wire is occupied by the solitons or patterns. States with $I_D < 10^{-10}$ are assumed to be uniform ones, while those with $I_D > 10^{-2}$ are considered as patterns.

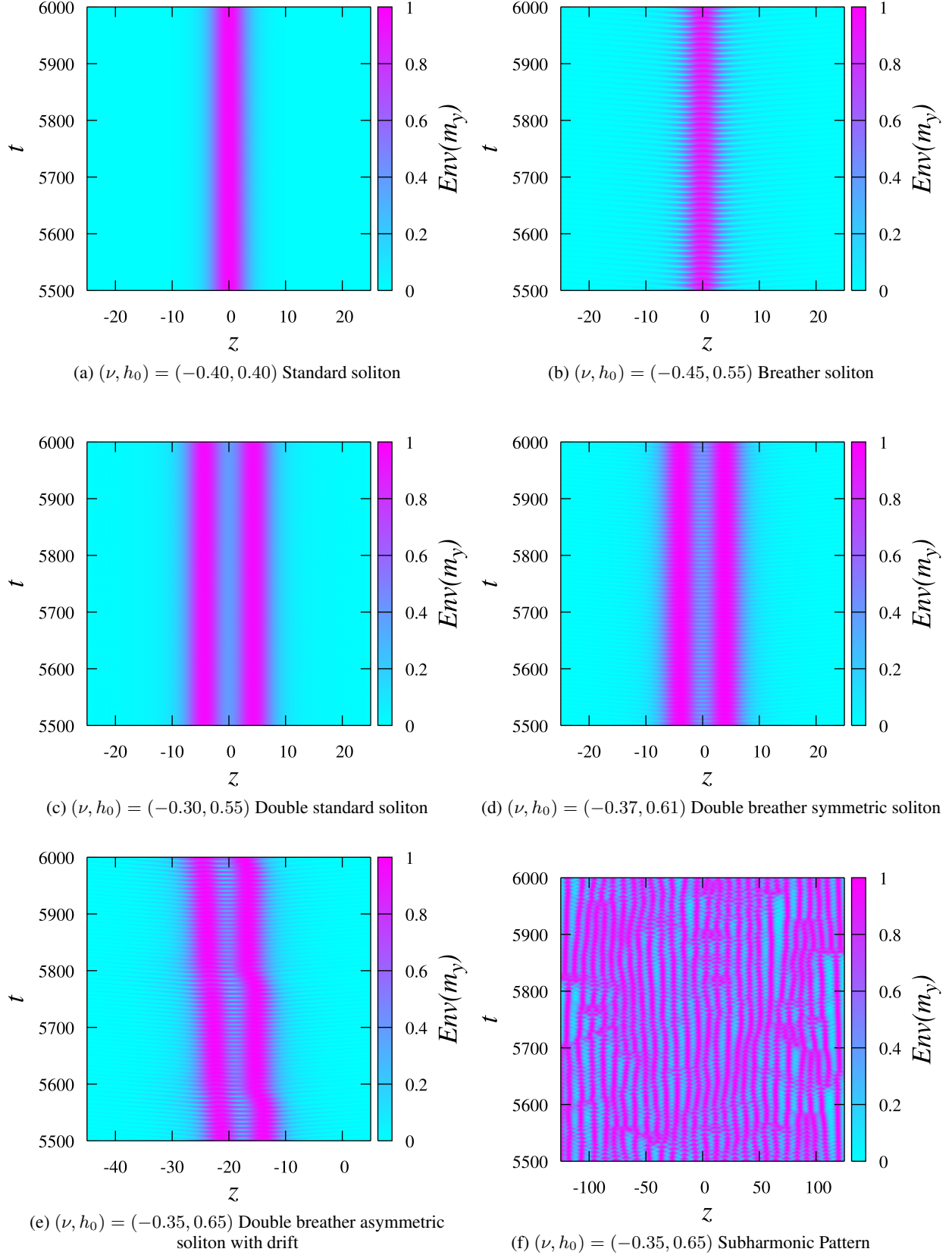


Figure 2: (color online) Envelopes of different responses of the magnetic wire, defined as per Eq. (9) and plotted as $m_y(z, t_i)$, with t_i being time moments at which the spatial average of $m_y(z, t)$ has a local maximum. Therefore, the color maps capture the dynamics only for the long timescale.

While considering the steady-state stage, in the course of interval $t \in [5000, 6000]$, attention was again focused the m_y component. The short-timescale dynamics of \mathbf{m} in response to the external field modulation was eliminated by computing the envelope of m_y . The evolution of the envelope is represented by values $m_y(z, t_i)$, where t_i are time points maximizing the space average of m_y ,

$$\langle m_y \rangle(t) = \frac{1}{2L} \int_{-L}^{+L} m_y(z, t) dz. \quad (9)$$

Thus, only variations of the response amplitude on the long timescale are taken into account. Figure 2 shows examples of the envelope evolution for different responses observed at the steady-state stage for different values of the control parameters, (ν, h_0) . Panels (a) and (b) show the standard single-soliton and breather regimes, which are similar to those previously reported in Ref. Urzagasti et al. [2012]. Panel (c) shows an example of the standard two-soliton pair. In that case, individual solitons in the pair keep the amplitude and width similar to those of the single-soliton states.

On the other hand, panels (d) and (e) in Fig. 2 display novel double-breather soliton solutions, whose amplitudes oscillate on the long timescale, unlike the non-breathing solitons, which remain completely stationary. Both single- and double-breather solitons emit radiation. Furthermore, the double breather in panel (e) in Fig. 2 is drifting away from its initial position, which is closely related to the noticeable breaking of its inner symmetry. The drift is exhibited by all double-breather solitons (it is not visible in panel (d), as the timescale is not long enough for that). Indeed, the asymmetric emission of radiation resulting from the spontaneously emerging asymmetry in the structure of the soliton complexes gives rise to unequal left and right recoil forces, which drives the drift. Finally, panel (f) in Fig. 2 shows an example of the dynamical regime in which the entire wire is occupied by an apparently randomized subharmonic pattern.

In the steady stage, the CM position of the envelope was defined in the same way as in Eq. (7), with the difference that here we consider only time moments t_i at which $\langle m_y \rangle(t)$ has a maximum. The average CM velocity is then estimated, as said above, by means of the linear fit to $z_{\text{CM}}(t_i)$. To provide a simple criterion distinguishing single and double solitons in the response, the time average of the centered envelope,

$$\bar{m}_{\text{env}}(z) = \frac{1}{n} \sum_{i=1}^n m_y(z - z_{\text{CM}}(t_i), t_i) \quad (10)$$

was computed. In the framework of the time-averaging procedure, the radiation waves emitted by the breathers were flattened, and the number of solitons was identified by directly counting the number of local-maximum points in the $\langle m_y \rangle(z)$ profile.

Regardless of the number of solitons, the distinction between fundamental ones and breathers was determined by computing the normalized power spectral density (PSD) of $\langle m_y \rangle(t)$, i.e., the squared absolute value of the complex fast Fourier transform, normalized to its maximum. Figure 3 presents plots of both $\langle m_y \rangle(t)$ and its PSD corresponding to the same responses which are displayed in Fig. 2. In the usual regimes (panels (a) and (c)), the soliton's oscillation amplitude remains constant, and the PSD exhibits a global peak at $\omega = \Omega/2$ (i.e., half the driving frequency in the parametrically forced equation (3)), as the response is subharmonic, and it also exhibits lower peaks at odd multiples of $\Omega/2$. If the breathing is present (panels (b) and (d)), the soliton's size varies on the long timescale, and PSD exhibits a multitude of low peaks agglomerated around the odd multiples of $\Omega/2$, representing a large set of oscillation modes. The simple peak count makes it possible to conclude if the breathing is present or not in the dynamical regime. To this end, only the peaks at frequencies $\omega < 3\Omega$ are considered, as peaks beyond this range are extremely weak.

The microscopically defined magnetic free energy Q of the system is the sum of the exchange energy, anisotropy energy, and the energy of the interaction with the external magnetic field Bertotti et al. [2009], i.e.,

$$Q = \frac{1}{2L} \int_{-L}^{+L} \left(\frac{1}{2} (\partial_z \mathbf{m})^2 - \frac{\beta}{2} (1 - m_z^2) - \mathbf{h} \cdot \mathbf{m} \right) dz. \quad (11)$$

The last dynamical indicator employed in our analysis is the largest Lyapunov exponent (LLE), λ_{max} , which provides a deeper understanding of the dynamical system. In particular, λ_{max} determines the average exponential rate of divergence or convergence of neighboring orbits in the system's phase space. Thus, condition $\lambda_{\text{max}} > 0$ delineates a region of chaotic dynamics, suggesting rapid loss of the system's predictability, which is the hallmark of dynamical chaos. The magnitude of positive λ_{max} defines the timescale on which the dynamics become unpredictable. Conversely, exponential convergence, corresponding to $\lambda_{\text{max}} < 0$, indicates stability of periodic orbits. In the neutral case, $\lambda_{\text{max}} \approx 0$, the system is defined as a marginally stable or quasi-periodic one.

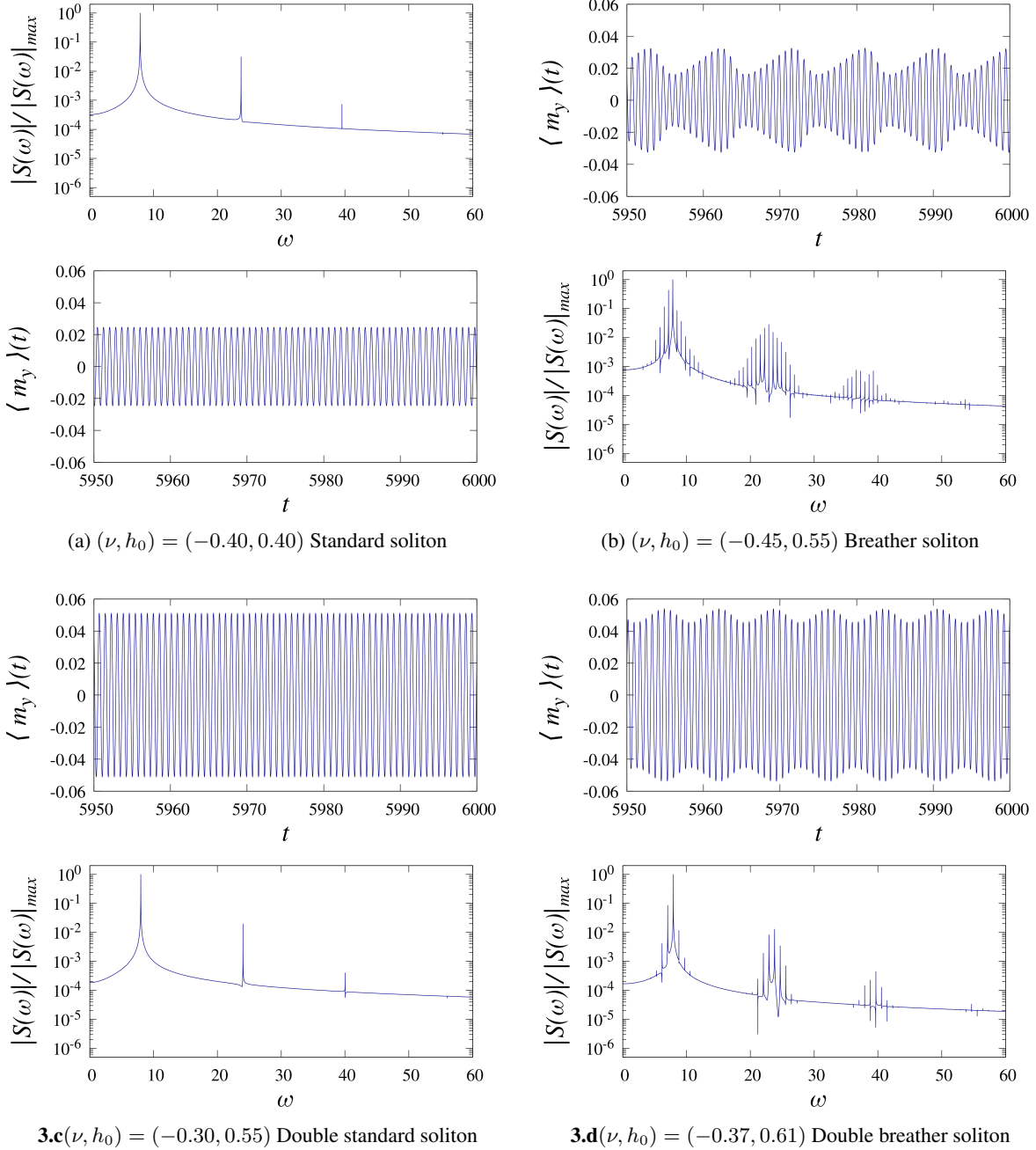


Figure 3: Plots of the spatial average of $m_y(x, t)$, defined as per Eq. (9) and its normalized power spectral density (PSD) for the soliton regimes displayed in Fig. 2. The standard soliton states exhibit the spatial average oscillating with a constant amplitude, and, accordingly, PSD with well-defined peaks at odd multiples of the main oscillation frequency, $\omega = \Omega/2$, which is imposed by the parametric drive in Eq. (3). In breather solitons, the oscillation amplitude of the spatial average varies on the long timescale, which translates into PSD with multiple frequency peaks.

The LLE can be calculated as Wolf et al. [1985],

$$\lambda_{\max} = \lim_{t \rightarrow \infty} \frac{1}{t} \ln \frac{\|\delta \mathbf{m}(z, t)\|}{\|\delta \mathbf{m}(z, t_0)\|}, \quad (12)$$

where $\|\bullet\| \equiv (\int_{-L}^{+L} |\bullet|^2 dz)^{1/2}$. The vector function $\delta \mathbf{m}$ in Eq. (12), which represents the distance in the phase space between close orbits, obeys the linear equation,

$$\frac{\partial(\delta \mathbf{m})}{\partial t} = \bar{\mathbf{J}} \cdot \delta \mathbf{m}, \quad (13)$$

where $\bar{\mathbf{J}}$ is the Jacobian matrix of Eq. (1). In our numerical analysis, λ_{\max} was calculated from $t_0 = 6 \times 10^3$ up to $t_{\max} = 2 \times 10^4$. At each time step, $\|\delta \mathbf{m}(z, t)\|$ was rescaled to restore its initial norm, $\|\delta \mathbf{m}(z, t_0)\|$. Finally, λ_{\max} is evaluated as the average value between times $t = 1.8 \times 10^4$ and $t = 2.0 \times 10^4$. Let us comment that this method is the most common one used in the literature to characterize chaotic states Sano and Sawada [1985], Ramasubramanian and Sriram [2000], Rosenstein et al. [1993], Geist et al. [1990], Pati [2024], Mazanik et al. [2024], Bazzani et al. [2023], Field et al. [2021], Zhao and Zhang [2024].

5 Results

5.1 Existence regions

Figure 4(a) summarizes all localized-state responses in the (ν, h_0) map for the initial condition given by Eqs. (6). The existence regions lie right under the boundary of the first Arnold tongue, above which the system exhibits only delocalized patterns covering the entire spatial domain. Among the existence regions, the lowest and largest ones are those where the system responds with the creation of a standard single soliton (1–pink) or a single breather soliton (2–purple). Both regions are significantly larger than their counterpart found in Ref. Urzagasti et al. [2014b], almost doubling their area. This happens because a different initial condition, in the form of a simple soliton, was used in that work. Surprisingly enough, such initial condition falls outside the attraction basin of the single-soliton response for lower values of h_0 , yet the double-soliton initial condition, defined above by Eqs. (6), belongs to the respective basin.

On the other hand, the double-soliton initial condition does produce a stable double-soliton response above the aforementioned regions, still under the boundary of the Arnold tongue, between $\nu = -0.5$ and $\nu = 0.2$. Three regions are distinguished here. In the middle one (3–orange), the double soliton is of the usual type, with no breathing, while near the lower-left border and in the upper part (4–red) the double soliton exhibits breathing (thus this response is found in the disconnected set). Some of these modes exhibit the drift at a relatively small velocity. The region in the upper-left corner (5–blue) corresponds to the responses that are identified as fast-drifting localized structures, according to the measurement of their CM velocity, as outlined at the beginning of section 4. Here, the system exhibits breathing double solitons. Drifting at larger velocities, they hit edges of the spatial domain, during either the transient stage of the steady one. The simulations reveal that, as a result of hitting the edge, the double soliton stays stuck near the edge for an uncertain time, and then drifts back. In the double-soliton regions, the single-soliton initial condition still leads to the stable single-soliton responses Urzagasti et al. [2014b], which implies the system's multistability, as the single- and double-soliton regimes coexist with each other and with the uniform state, $\mathbf{m} = \hat{x}$.

An unexpected response was observed in a very small region around $(\nu, h_0) = (-0.20, 0.45)$, just under the Arnold tongue (region 6–green in Fig. 4(a)). Here, the system exhibits a localized intermittent state where a small region in the wire is filled by solitons that varies in time, as they may spontaneously appear, disappear or collide. Figure 5(a) illustrates an example of the intermittent state. The two initially launched solitons collide and merge into a single soliton, which suddenly splits in a set of seven solitons, that occupy the region between $z = -50$ and $z = +50$ with a relatively smooth distribution. Shortly afterwards, the solitons drift towards the center, leading to disappearance of the central soliton, and thus decreasing the soliton number to six. Next, two adjacent solitons collide and merge, which further reduces the number to five. As the solitons keep drifting to the center, the above-mentioned soliton, produced by the merger, also disappears while two others, adjacent to it, collide and merge once again. The remaining three solitons become closer and suddenly split in seven ones, then repeating the cycle of the solitons metamorphoses. This dynamical regime is very robust and regular in its evolution. It is spatially symmetric and does not exhibit a global drift. The regularity of this regime is also confirmed in Fig. 5(b) by the respective picture of the evolution of the spatial average $\langle m_y \rangle(t)$, as well as by its PSD. As the number of solitons decreases by steps, so does the oscillation amplitude of $\langle m_y \rangle(t)$, while the regime remains periodic on the long timescale, covering the entire cycle of the metamorphoses. The corresponding PSD exhibits pronounced peaks at the subharmonic response frequency $\omega = \Omega/2$, as well as its odd multiples, similar to the regimes based on single and double standard solitons, which are outlined above.

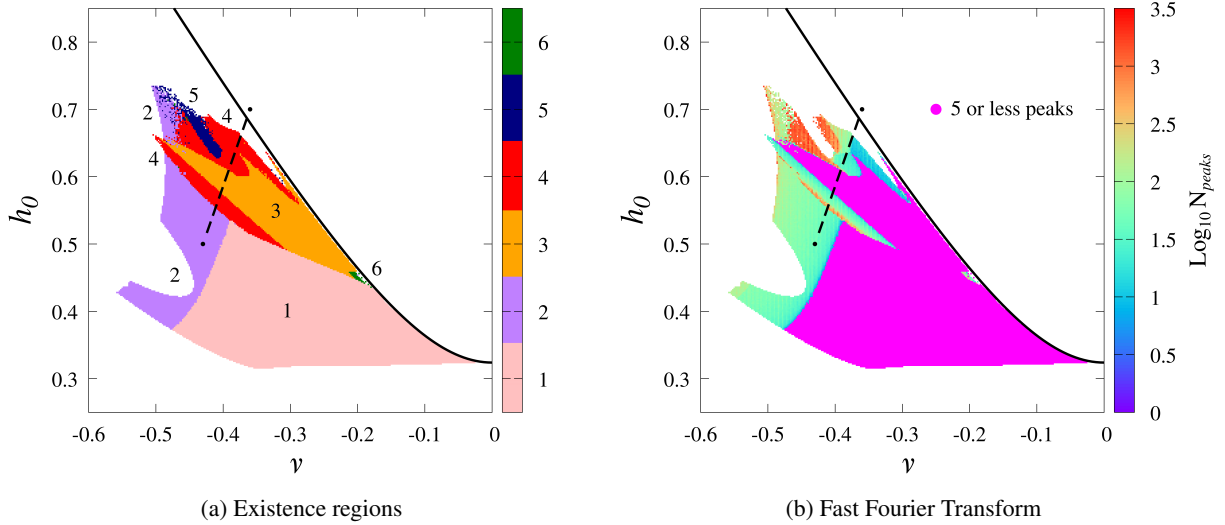


Figure 4: (color online) **(a)** Existence regions in the (ν, h_0) parameter plane. The regions are found for the following six states: simple solitons (1–pink), breather solitons (2–purple), double solitons (3–orange), double breather solitons (4–red), fast-moving localized structures (5–blue), and intermittent localized states (6–green). **(b)** Number of peaks in the case of $\omega = 3\Omega$, as produced by the fast Fourier transform. In both panels, the solid line is the boundary of the first Arnold tongue. The modes belonging to the dashed line, $h_0(\nu) = 2.857\nu + 1.729$, ranging from $(\nu, h_0) = (-0.43, 0.5)$ to $(\nu, h_0) = (-0.36, 0.7)$, is considered by means of the detailed study of the micromagnetic energy and largest Lyapunov exponent in subsections 5.4 and 5.5, respectively.

The boundaries between the existence regions of localized states plotted in Fig. 4 are well defined in most cases, except for the upper-left corner, where the boundaries are fuzzy. The reason for the fuzziness is that, as mentioned above, stability regions of the respective solutions overlap, and the multistability takes place. As the attraction basins are different for different areas in the (ν, h_0) plane, the initial condition given by Eqs. (6) evolves towards different attractors. The fuzzy boundaries involve breathing solutions only, suggesting that the true attraction basins may have a fractal structure, and the attractors are chaotic Nieto et al. [2020], Bernal et al. [2020], Daza et al. [2023].

In the rest of the region under the Arnold tongue, the system responds with either a spatially uniform state or delocalized patterns.

5.2 The power spectral density

Panel (b) in Fig. 4 shows the number of peaks in the power spectral density from $\omega = 0$ to $\omega = 3\Omega$ in the existence regions of localized states in the (ν, h_0) plane. There is a large region with a reduced number of peaks (≤ 5). This region coincides with the union of those where the system exhibits either a single soliton or double standard ones in Fig. 4(a). The chart is in agreement with the examples displayed in Figs. 3(a,c). Single- and double-soliton regimes with no breathing feature only three peaks at $\omega = \frac{1}{2}\Omega$, $\omega = \frac{3}{2}\Omega$ and $\omega = \frac{5}{2}\Omega$ (with some additional tiny peaks arising as the level of the numerical errors). On the other hand, the number of peaks is suddenly increased in the breather-soliton regions. Most of the single-breather-soliton region features the number of peaks $\sim 50 - 100$. In most of the lower-left double-breather region, the results are similar. In the upper-right double-breather region, four well-delimited zones can be recognized, where the numbers of peaks are on the order of 1, 10 and 100. The last of these zones surround the region of fast-drifting localized modes, where, the number of peaks is counted in hundreds and thousands, with a maximum of ≈ 3200 peaks. This is also consistent with the examples displayed in Figs. 3 (b,d).

5.3 The center-of-mass (CM) drift of solitons

Figure 6 summarizes indicators related to the CM mobility of the soliton structure, at different values of (ν, h_0) . For each point of the map, the time series $z_{\text{CM}}(t_i)$, accounting for the CM position, is extracted from the envelope data in the course of the steady-state stage (i.e., at $t_i \in [5000, 6000]$), and the following dynamical indicators are computed. The absolute value of the average CM velocity, which is estimated as the slope of the linear fit for $z_{\text{CM}}(t_i)$, is shown in panel (a). The departure of the velocity from its average is estimated as the standard deviation of the linear-fit slope, considering $z_{\text{CM}}(t_i)$ terms as normally-distributed random variables Press et al. [1993]. The deviation is shown in

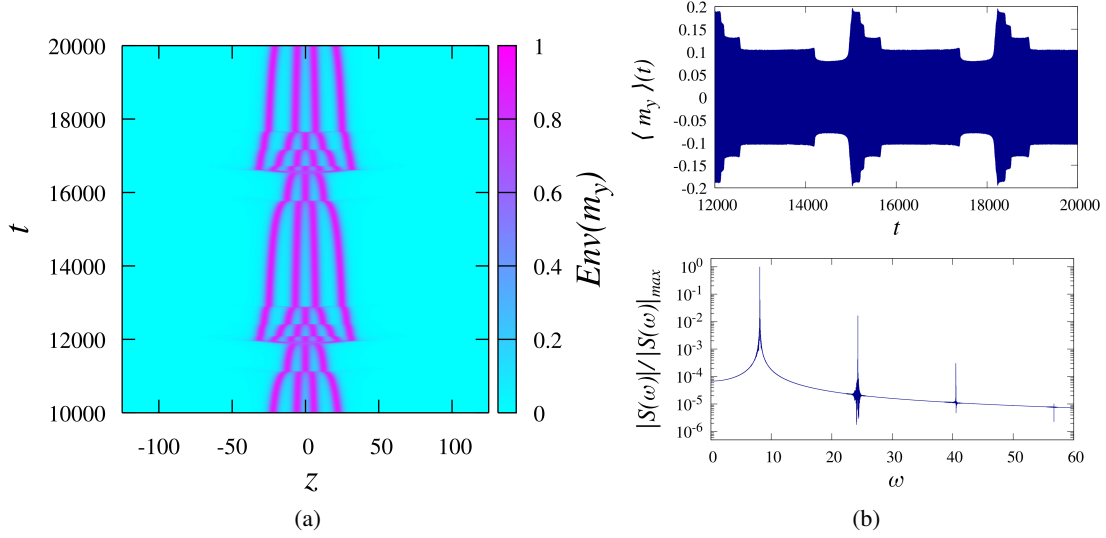


Figure 5: (color online) The response of the system for $(\nu, h_0) = (-0.20, 0.45)$ in the form of an intermittent localized state. (a) Envelope $m_y(z, t_i)$. (b) The spatial average of $m_y(x, t)$ and its normalized power spectral density (PSD).

panel (b). The absolute value of the time-average CM position and its standard deviation are shown in Figs. 6(c) and (d), respectively.

In Fig. 6, four well-delimited zones can be identified in terms of these dynamical indicators. Zone 1 (in purple) is the largest one, encompassing all usual-single-soliton regimes, almost all single-breathing-soliton ones, almost all regimes of usual double solitons, and most cases of double breathing solitons. Here, the average soliton speed is $\lesssim 10^{-12}$, the other indicators exhibiting extremely low values too, which may be regarded as zero for all practical purposes. Zone 2 is a disconnected set at the upper-left corner of Fig. 6. It includes a narrow edge occupied by single breathing solitons under (but disconnected from) a narrow edge occupied by the usual double solitons, whose left end is connected to the lower end of the edge occupied by single breathing solitons. The solitons in this zone exhibit average speeds $\sim 10^{-6}$ with deviations $\sim 10^{-9}$. Such speeds imply a displacement $\sim 10^{-3}$ during the steady stage, which is much smaller than the mesh size $dz = 1/6$ of the numerical scheme. Therefore, these solitons are also regarded as non-drifting ones. However, the average displacement of the solitons from $z = 0$ ranges between 0.1 and 10. This occurs because, although the solitons do not drift during the steady-state stage, they do so during the preceding transient stage, thus producing an initial position at the beginning of the steady-state stage far from $z = 0$.

Zone 3 is the right diagonal end of the breathing double-soliton region. It has the same features as zone 2 in terms of the average drift speed, but the average CM position is closer to zero (with a distance $\sim 10^{-4}$), which means that the CM remains close to $z = 0$ in the course of both the transient and steady-state stages. On the other hand, both the CM position and CM velocity exhibit larger, yet still small deviations, $\sim 10^{-1}$ and 10^{-5} , respectively. These tiny fluctuations are caused by the complexity of the breathing double-soliton structure. Zone 4 is located at the upper-left corner in Fig. 6, around the region of the fast-moving localized modes, see Fig. 4(a). It is occupied exclusively by the breathing double solitons, being the *only zone* that exhibits non-negligible drift. The respective drift speeds exhibit average values in the range of 10^{-4} to 10^{-1} , with a maximum average speed found to be 0.032, which allows the double breather to travel the distance of 32.0 during the steady-state stage. Considering that the average CM positions have absolute values in the range of 1 to 10, with a maximum of 39.28, which implies that the double breathers remain far enough from the wire's edges at $z = \pm 125$. All in all, some double breathers exhibit the persistent drift with an almost constant velocity, while others move with a sign-changing (oscillating) velocity.

5.4 The micromagnetic energy

Figure 7(a) summarizes the computation of the maximum value of the micromagnetic free energy along the line which was shown above in Fig. 4, defined as $h_0(\nu_{h_0}) = 2.857\nu_{h_0} + 1.729$ and ranging between points $(\nu, h_0) = (-0.43, +0.5)$ and $(\nu, h_0) = (-0.36, +0.7)$. For 2048 points uniformly distributed along the line, the peak values of the time series for the energy were found. Along the line, a number of segments can be identified in terms of the peak energies. First, in the segment $0.5 < h_0 < 0.553$, the peak energies increase with a uniform slope of ≈ 0.98 , always lying in a

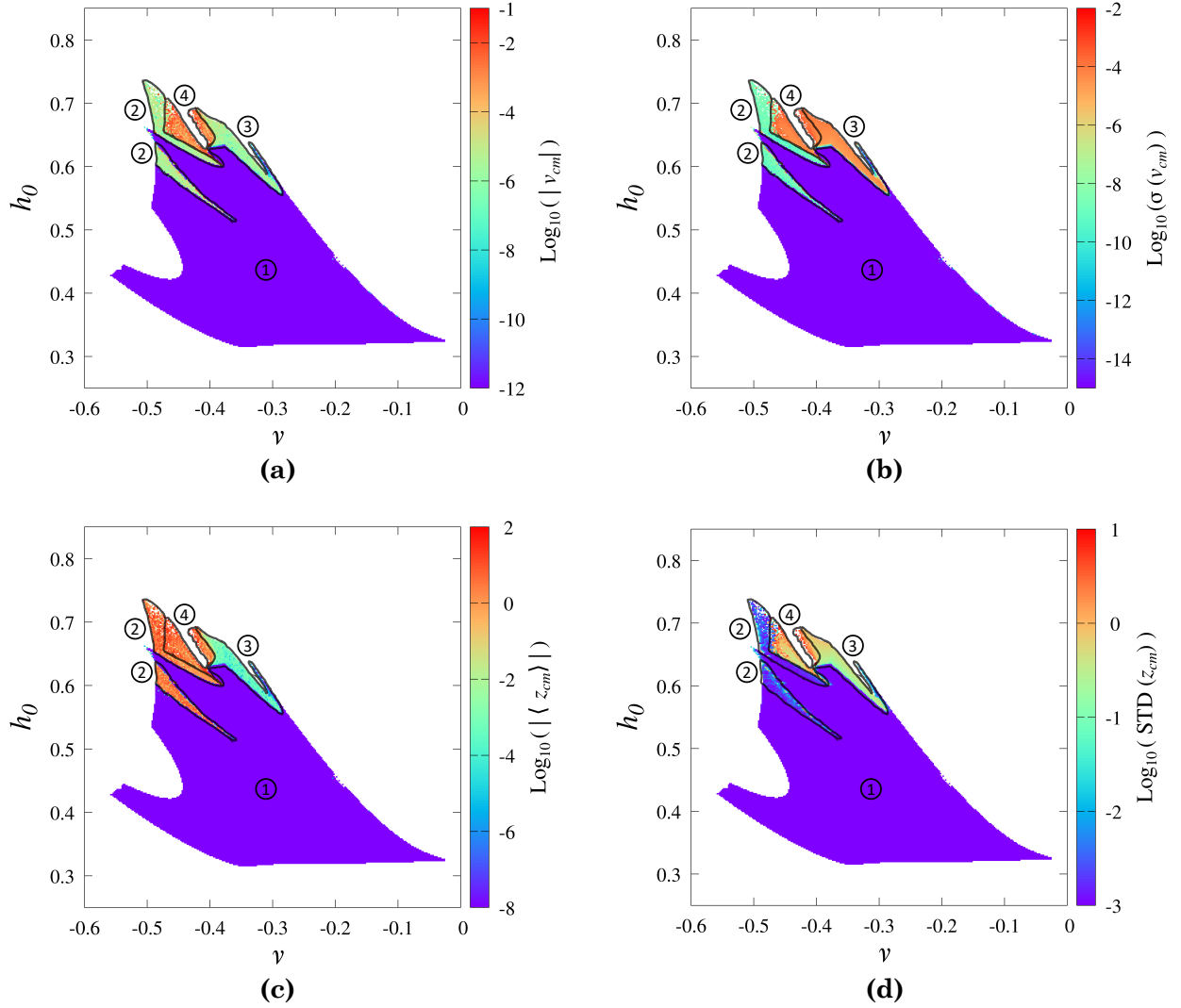


Figure 6: (color online) Dynamical indicators related to the center of mass (CM) of the soliton patterns, in the (ν, h_0) plane, plotted on the logarithmic scale. (a) The absolute value of the average CM velocity. (b) The deviation of the CM velocity from its average value. (c) The absolute value of the average CM position. (d) The standard deviation (STD) of the CM position. Four well-delimited zones, designated by different colors, are identified, in terms of these dynamical indicators.

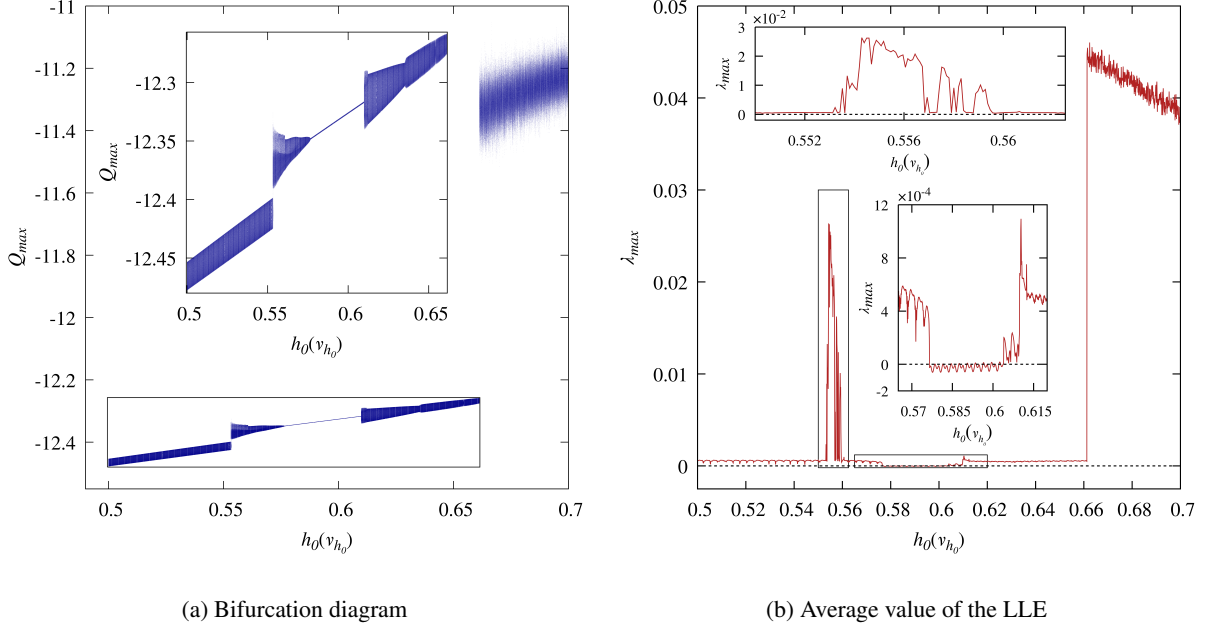


Figure 7: Bifurcation diagrams plotted along the line $h_0(\nu_{h_0}) = 2.857\nu_{h_0} + 1.729$. **(a)** Local maximum values of the micromagnetic free energy. **(b)** The average value of the largest Lyapunov exponent. Insets in each panel zoom the framed areas of the corresponding diagrams.

band of width $\Delta Q = 0.025$. This segment is the one where the line passes through the lower region of the breathing single solitons. At $h_0 \approx 0.553$, there is a sudden increase in the peak energies, as the line is now passing through the region of the breathing double solitons. The energy increases here, as a longer section of the wire is now occupied by the excited state. As h_0 grows, so do the peak energies, but the width of the band decreases. Close to $h_0 = 0.579$, the peak-energy branch becomes a line, which extends up to $h_0 = 0.609$ with a slope of ≈ 0.97 . This makes sense because the respective segment passes through the region of the standard (usual) double solitons. As the long-timescale dynamics remains steady, the peak energies are identical to one another. At $h_0 = 0.609$, the line enters the upper region populated by double breathing solitons, and the peak energies again appear as bands with a width that tends to increase with h_0 . All in all, the peak energies keep increasing with h_0 at a fairly constant rate. At $h_0 = 0.662$, the peak energies increase suddenly from about -12.3 to -11.3 , as the line enters the region where the system switches into the subharmonic pattern, the entire wire being now occupied by the excited state.

5.5 The largest Lyapunov exponent (LLE)

The LLE was computed for the same set of 2048 points along the same line plotted in Fig. 4). The results are summarized in Fig. 7(b). Similar to the peak energies, changes in the LLE along the line can be associated with its segments traversing different existence regions, see Fig. 4(a). For $h_0 \in [0.5, 0.553]$, in the region of the breathing single solitons, the LLE shows values $\sim 10^{-4}$. These small positive values imply that the system is weakly chaotic in this case. Similar LLE values are observed for $h_0 \in [0.561, 0.579]$, in the lower region of the breathing double solitons. Between these two intervals, i.e., at $h_0 \in [0.553, 0.561]$, the LLE exhibits much larger values, up to 0.026. This part of the line covers the lower edge of the lower region of the breathing double solitons, where the respective PSD exhibits significantly more peaks than in the rest of the region (about 10 times more, as shown in Fig. 4(b)). This difference is related to the drastic increase in the LLE values in this segment. For $h_0 \in [0.579, 0.604]$, in the region of usual double solitons, the LLE takes negative values $\sim -10^{-5}$. This means that the usual double-soliton states are non-chaotic. For $h_0 \in [0.604, 0.662]$, in the upper region of the breathing double solitons, the LLE takes positive values $\sim 5 \times 10^{-4}$. At $h_0 > 0.662$, in the region of the subharmonic patterns, the LLE drastically increases to about 0.045, which is expected, given the chaotic shape of these patterns occupying the entire wire. All in all, the LLE analysis shows that the dynamics of the usual solitons is regular (non-chaotic), while it is chaotic for the breathing solitons, and subharmonic patterns are chaotic too. This is consistent with the results for single solitons reported in Ref. Urzagasti et al. [2013].

6 Conclusions

The subject of this work is the systematic study of dynamical regimes in the one-dimensional rectilinear magnetic wire modeled by the LLG (Landau-Lifshitz-Gilbert) equation with the Neumann's boundary conditions, driven by the spatially uniform magnetic field, including DC and AC components, which is directed perpendicular to the wire. The AC parametric drive maintains magnetic excitations at the subharmonic frequency. By means of the systematic numerical analysis, which includes the computation of PSD (power spectral density) with the help of the Fourier transform, areas in the parameter plane of the drive's amplitude and frequency detuning from the parametric resonance are identified, in which the driven LLG equation supports different robust localized dynamical states. These include usual single- and double-soliton modes, single and double breathers (which emit small-amplitude dispersive waves), fast-moving modes, and intermittent multi-soliton complexes, which exhibit periodic metamorphoses with the change in the number of solitons. The results reveal the presence of multistability in the system, which includes the coexistence of stable localized states and delocalized ones that cover the entire wire. Basic dynamical characteristics of these states are found, such as the average magnetization, LLE (largest Lyapunov exponent), and velocity of the CM (center of mass) drift, in the case of the double breathers with spontaneously broken inner symmetry. The states with negative and positive values of LLE feature, respectively, regular and chaotic evolution.

The dynamical states addressed in the present work do not exhaust the variety of complex modes that the LLG equation may generate. More sophisticated states, such as multisoliton bound states, may be a subject for further investigation.

It may also be relevant to extend the work by considering the model based on the LLG equation with periodic boundary conditions, corresponding to the ring-shaped magnetic wire. Besides, it may be interesting to study collisions between the fast-moving modes. In these cases, a comparison with the simplified model based on the PDNLS (parametrically-driven damped nonlinear Schrödinger) equation can help to establish the universality of the phenomena. A challenging possibility is to develop a two-dimensional version of the setting. Indeed, it is known that many models predict the existence of stable two-dimensional solitons maintained by the balance of gain and loss (see, e.g., Ref. Yin et al. [2023]).

Acknowledgments

The work of B.A.M. was supported, in part, by the Israel Science Foundation through grant No. 1695/22. PD and DL acknowledge partial financial support from FONDECYT 1231020. We thank Mr. Manuel J. Suazo from University of Tarapacá for his valuable advice to implement the parallelization in our numerical algorithms. DL acknowledges the hospitality of *Université Côte d'Azur* (Nice, France) and *Universidad Nacional de San Agustín* (Arequipa, Perú) where part of this work was written.

Abbreviations

The following abbreviations are used in this manuscript:

LLG	Landau-Lifshitz-Gilbert
PSD	Power Spectral Density
LLE	Largest Lyapunov Exponent
CM	Center of Mass

References

- Igor S. Aranson and Lorenz Kramer. The world of the complex ginzburg-landau equation. *Rev. Mod. Phys.*, 74:99–143, Feb 2002. doi:10.1103/RevModPhys.74.99. URL <https://link.aps.org/doi/10.1103/RevModPhys.74.99>.
- Nikolay N. Rosanov. *Spatial Hysteresis and Optical Patterns*. Springer Series in Synergetics. Springer, Berlin, Heidelberg, 2013. doi:10.1007/978-3-662-04792-7.
- L. A. Lugiato and R. Lefever. Spatial dissipative structures in passive optical systems. *Phys. Rev. Lett.*, 58:2209–2211, May 1987. doi:10.1103/PhysRevLett.58.2209. URL <https://link.aps.org/doi/10.1103/PhysRevLett.58.2209>.
- Y.V. Kartashov, O. Alexander, and D.V. Skryabin. Multistability and coexisting soliton combs in ring resonators: the lugiato-lefever approach. *Opt. Express*, 25(10):11550–11555, May 2017. doi:10.1364/OE.25.011550. URL <https://opg.optica.org/oe/abstract.cfm?URI=oe-25-10-11550>.

- John W Miles. Parametrically excited solitary waves. *Journal of Fluid Mechanics*, 148:451–460, 1984.
- I. V. Barashenkov, M. M. Bogdan, and V. I. Korobov. Stability diagram of the phase-locked solitons in the parametrically driven, damped nonlinear schrödinger equation. *Europhysics Letters*, 15(2):113, may 1991. doi:10.1209/0295-5075/15/2/001. URL <https://dx.doi.org/10.1209/0295-5075/15/2/001>.
- Michael Faraday. Xvii. on a peculiar class of acoustical figures; and on certain forms assumed by groups of particles upon vibrating elastic surfaces. *Philosophical transactions of the Royal Society of London*, (121):299–340, 1831.
- Alwyn C Scott. A nonlinear klein-gordon equation. *American Journal of Physics*, 37(1):52–61, 1969.
- P Couillet, T Frisch, and G Sonnino. Dispersion-induced patterns. *Physical Review E*, 49(3):2087, 1994.
- MG Clerc, Saliya Coulibaly, and D Laroze. Interaction law of 2d localized precession states. *Europhysics Letters*, 90(3):38005, 2010a.
- IV Barashenkov, EV Zemlyanaya, and TC Van Heerden. Time-periodic solitons in a damped-driven nonlinear schrödinger equation. *Physical Review E—Statistical, Nonlinear, and Soft Matter Physics*, 83(5):056609, 2011.
- NV Alexeeva, IV Barashenkov, and GP Tsironis. Impurity-induced stabilization of solitons in arrays of parametrically driven nonlinear oscillators. *Physical review letters*, 84(14):3053, 2000.
- IV Barashenkov and EV Zemlyanaya. Stable complexes of parametrically driven, damped nonlinear schrödinger solitons. *Physical review letters*, 83(13):2568, 1999.
- Elena Valerievna Zemlyanaya and NV Alexeeva. Oscillating solitons of the driven, damped nonlinear schrödinger equation. *Theoretical and Mathematical Physics*, 159:870–876, 2009.
- IV Barashenkov and EV Zemlyanaya. Soliton complexity in the damped-driven nonlinear schrödinger equation: Stationary to periodic to quasiperiodic complexes. *Physical Review E—Statistical, Nonlinear, and Soft Matter Physics*, 83(5):056610, 2011.
- D. Urzagasti, D. Laroze, M. G. Clerc, S. Coulibaly, and H. Pleiner. Two-soliton precession state in a parametrically driven magnetic wire. *Journal of Applied Physics*, 111(7):07D111, 02 2012. ISSN 0021-8979. doi:10.1063/1.3672872. URL <https://doi.org/10.1063/1.3672872>.
- VS Shchesnovich and IV Barashenkov. Soliton–radiation coupling in the parametrically driven, damped nonlinear schrödinger equation. *Physica D: Nonlinear Phenomena*, 164(1-2):83–109, 2002.
- Vladimir Igorevich Arnold. *Geometrical methods in the theory of ordinary differential equations*, volume 250. Springer Science & Business Media, 2012.
- Marcel G. Clerc, Saliya Coulibaly, and David Laroze. Parametrically driven instability in quasi-reversal systems. *International Journal of Bifurcation and Chaos*, 19(10):3525–3532, 2009a. doi:10.1142/S0218127409024967. URL <https://doi.org/10.1142/S0218127409024967>.
- Atsushi Okamura and Hidetoshi Konno. Resonant breakup of soliton in parametrically driven nonlinear schrödinger equation. *Journal of the Physical Society of Japan*, 58:1930–1933, 1989. doi:10.1143/JPSJ.58.1930. URL <https://api.semanticscholar.org/CorpusID:123368473>.
- Bruce Denardo, Brian Galvin, Alan Greenfield, Andrés Larraza, Seth Putterman, and William Wright. Observations of localized structures in nonlinear lattices: Domain walls and kinks. *Phys. Rev. Lett.*, 68:1730–1733, Mar 1992. doi:10.1103/PhysRevLett.68.1730. URL <https://link.aps.org/doi/10.1103/PhysRevLett.68.1730>.
- Mariana Bondila, Igor V. Barashenkov, and Mikhail M. Bogdan. Topography of attractors of the parametrically driven nonlinear schrödinger equation. *Physica D: Nonlinear Phenomena*, 87(1):314–320, 1995. ISSN 0167-2789. doi:10.1016/0167-2789(95)00126-O. URL <https://www.sciencedirect.com/science/article/pii/0167278995001260>. Proceedings of the Conference on The Nonlinear Schrodinger Equation.
- I. V. Barashenkov and Yu. S. Smirnov. Existence and stability chart for the ac-driven, damped nonlinear schrödinger solitons. *Phys. Rev. E*, 54:5707–5725, Nov 1996. doi:10.1103/PhysRevE.54.5707. URL <https://link.aps.org/doi/10.1103/PhysRevE.54.5707>.
- A.M. Cabanas, J.A. Vélez, L.M. Pérez, P. Díaz, M.G. Clerc, D. Laroze, and B.A. Malomed. Dissipative structures in a parametrically driven dissipative lattice: Chimera, localized disorder, continuous-wave, and staggered states. *Chaos, Solitons & Fractals*, 146:110880, 2021a. ISSN 0960-0779. doi:<https://doi.org/10.1016/j.chaos.2021.110880>. URL <https://www.sciencedirect.com/science/article/pii/S0960077921002332>.
- I. V. Barashenkov, S. Cross, and Boris A. Malomed. Multistable pulselike solutions in a parametrically driven ginzburg-landau equation. *Phys. Rev. E*, 68:056605, Nov 2003. doi:10.1103/PhysRevE.68.056605. URL <https://link.aps.org/doi/10.1103/PhysRevE.68.056605>.

- Hidetsugu Sakaguchi and Boris A. Malomed. Solitary pulses and periodic waves in the parametrically driven complex ginzburg-landau equation. *Journal of the Physical Society of Japan*, 72(6):1360–1365, 2003. doi:10.1143/jpsj.72.1360.
- LI Reyes, LM Pérez, L Pedraja-Rejas, P Díaz, J Mendoza, J Bragard, MG Clerc, and D Laroze. Characterization of faraday patterns and spatiotemporal chaos in parametrically driven dissipative systems. *Chaos, Solitons & Fractals*, 186:115244, 2024.
- Alejandro O León, Marcel G Clerc, and Saliya Coulibaly. Traveling pulse on a periodic background in parametrically driven systems. *Physical Review E*, 91(5):050901, 2015.
- Alejandro O Leon, Ernesto Berríos-Caro, Alejandra León, and Marcel G Clerc. Faraday kinks connecting parametric waves in magnetic wires. *Communications in Nonlinear Science and Numerical Simulation*, 131:107841, 2024.
- Grégory Moille, Miriam Leonhardt, David Paligora, Nicolas Englebert, François Leo, Julien Fatome, Kartik Srinivasan, and Miro Erkintalo. Parametrically driven pure-kerr temporal solitons in a chip-integrated microcavity. *Nature Photonics*, pages 1–8, 2024.
- MM Bogdan and OV Charkina. Structure of soliton bound states in the parametrically driven and damped nonlinear systems. *Low Temperature Physics*, 48(12):1062–1070, 2022.
- Muzzamal Iqbal Shaukat, Montasir Qasymeh, and Hichem Eleuch. Spatial solitons in an electrically driven graphene multilayer medium. *Scientific Reports*, 12(1):10931, 2022.
- Ana M Cabanas, Ronald Rivas, Laura M Pérez, Javier A Vélez, Pablo Díaz, Marcel G Clerc, Harald Pleiner, David Laroze, and Boris A Malomed. A quasi-periodic route to chaos in a parametrically driven nonlinear medium. *Chaos, Solitons & Fractals*, 151:111089, 2021b.
- Deterlino Urzagasti, David Laroze, and Harald Pleiner. Two-dimensional localized chaotic patterns in parametrically driven systems. *Physical Review E*, 95(5):052216, 2017.
- D Urzagasti, David Laroze, and Harald Pleiner. Localized chaotic patterns in weakly dissipative systems. *The European Physical Journal Special Topics*, 223(1):141–154, 2014a.
- Juan F Marín, Rafael Riveros-Ávila, Saliya Coulibaly, Majid Taki, Leonardo Gordillo, and Mónica A García-Ñustes. Drifting faraday patterns under localised driving. *Communications Physics*, 6(1):63, 2023.
- Arthur Barbosa, Joao Pedro Sena, Najib Kacem, and Noureddine Bouhaddi. An artificial intelligence approach to design periodic nonlinear oscillator chains under external excitation with stable damped solitons. *Mechanical Systems and Signal Processing*, 205:110879, 2023.
- K Dileep and S Murugesh. Emergent soliton-like solutions in the parametrically driven 1-d nonlinear schrödinger equation. *Physica Scripta*, 98(4):045228, 2023.
- Pedro Parra-Rivas, Carlos Mas Arabi, and François Leo. Dissipative localized states and breathers in phase-mismatched singly resonant optical parametric oscillators: Bifurcation structure and stability. *Physical Review Research*, 4(1):013044, 2022.
- Nicolas Englebert, Francesco De Lucia, Pedro Parra-Rivas, Carlos Mas Arabí, Pier-John Sazio, Simon-Pierre Gorza, and François Leo. Parametrically driven kerr cavity solitons. *Nature Photonics*, 15(11):857–861, 2021.
- Sevastos Diamantidis, Theodoros P Horikis, and Nikos I Karachalios. Exciting extreme events in the damped and ac-driven nls equation through plane-wave initial conditions. *Chaos: An Interdisciplinary Journal of Nonlinear Science*, 31(5), 2021.
- Hiroshi Yamaguchi and Samer Hourri. Generation and propagation of topological solitons in a chain of coupled parametric-micromechanical-resonator arrays. *Physical Review Applied*, 15(3):034091, 2021.
- Franz G Mertens and Niurka R Quintero. Empirical stability criteria for parametrically driven solitons of the nonlinear schrödinger equation. *Journal of Physics A: Mathematical and Theoretical*, 53(31):315701, 2020.
- IV Barashenkov and Alexander Chernyavsky. Stable solitons in a nearly pt-symmetric ferromagnet with spin-transfer torque. *Physica D: Nonlinear Phenomena*, 409:132481, 2020.
- Héctor Urra, Juan F Marín, Milena Páez-Silva, Majid Taki, Saliya Coulibaly, Leonardo Gordillo, and Mónica A García-Ñustes. Localized faraday patterns under heterogeneous parametric excitation. *Physical Review E*, 99(3):033115, 2019.
- Yuval Edri, Ehud Meron, and Arik Yochelis. Spatial asymmetries of resonant oscillations in periodically forced heterogeneous media. *Physica D: Nonlinear Phenomena*, 410:132501, 2020.

- Michel A Ferré, Marcel G Clerc, Saliya Coulibally, René G Rojas, and Mustapha Tlidi. Localized structures and spatiotemporal chaos: comparison between the driven damped sine-gordon and the lugiato-lefever model. *The European Physical Journal D*, 71:1–8, 2017.
- Marcel G Clerc, Mónica A García-Ñustes, and Yair Zárate. Propagative phase shielding solitons in inhomogeneous media. *Physica D: Nonlinear Phenomena*, 269:86–93, 2014.
- Giorgio Bertotti, Isaak D. Mayergoyz, and Claudio Serpico. *Nonlinear Magnetization Dynamics in Nanosystems*. Elsevier Series in Electromagnetism. Elsevier, Oxford, 2009. doi:10.1016/B978-0-08-044316-4.00001-3. URL <https://www.sciencedirect.com/science/article/pii/B9780080443164000013>.
- Werner Scholz and Sharat Batra. Micromagnetic modeling of ferromagnetic resonance assisted switching. *Journal of Applied Physics*, 103:07F539–07F539, 03 2008. doi:10.1063/1.2838332.
- M. Lakshmanan. The fascinating world of the landau-lifshitz-gilbert equation: An overview. *Philosophical transactions. Series A, Mathematical, physical, and engineering sciences*, 369:1280–300, 03 2011. doi:10.1098/rsta.2010.0319.
- Eric Arturo Montoya, Salvatore Perna, Yu-Jin Chen, Jordan A Katine, Massimiliano d’ Aquino, Claudio Serpico, and Ilya N Krivorotov. Magnetization reversal driven by low dimensional chaos in a nanoscale ferromagnet. *Nature communications*, 10(1):543, 2019.
- Jean Bragard, JA Vélez, JA Riquelme, LM Pérez, Ruber Hernández-García, RJ Barrientos, and David Laroze. Study of type-iii intermittency in the landau–lifshitz-gilbert equation. *Physica Scripta*, 96(12):124045, 2021.
- Luis Fernandez Alvarez, Oscar Pla, and Oksana Chubykalo. Quasiperiodicity, bistability, and chaos in the landau-lifshitz equation. *Physical Review B*, 61(17):11613, 2000.
- Laura M Perez, Jean Bragard, Hector Mancini, Jason AC Gallas, Ana M Cabanas, Omar J Suarez, and David Laroze. Effect of anisotropies on the magnetization dynamics. *Networks and Heterogeneous Media*, 10(1):209–221, 2015.
- Ryan K Smith, Marek Grabowski, and RE Camley. Period doubling toward chaos in a driven magnetic macrospin. *Journal of magnetism and magnetic materials*, 322(15):2127–2134, 2010.
- JA Vélez, Jean Bragard, LM Pérez, AM Cabanas, OJ Suarez, David Laroze, and HL Mancini. Periodicity characterization of the nonlinear magnetization dynamics. *Chaos: An Interdisciplinary Journal of Nonlinear Science*, 30(9), 2020.
- Aaron M Feron and Robert E Camley. Nonlinear and chaotic magnetization dynamics near bifurcations of the landau-lifshitz-gilbert equation. *Physical Review B*, 95(10):104421, 2017.
- Ryan K Smith, Marek Grabowski, and RE Camley. Nonlinear behavior in magnetic transients. *Journal of magnetism and magnetic materials*, 321(20):3472–3477, 2009.
- DI Sementsov. Chaotic magnetization dynamics in single-crystal thin-film structures. *Crystallography Reports*, 54(1), 2009.
- AE Botha, Yu M Shukrinov, J Tekić, and MR Kolahchi. Chaotic dynamics from coupled magnetic monodomain and josephson current. *Physical Review E*, 107(2):024205, 2023.
- Laichuan Shen and Ka Shen. Skyrmion-based chaotic oscillator driven by a constant current. *Physical Review B*, 109(1):014422, 2024.
- Terufumi Yamaguchi, Sumito Tsunegi, Kohei Nakajima, and Tomohiro Taniguchi. Computational capability for physical reservoir computing using a spin-torque oscillator with two free layers. *Physical Review B*, 107(5):054406, 2023.
- Vivek Unikandanunni, Rajasekhar Medapalli, Marco Asa, Edoardo Albisetti, Daniela Petti, Riccardo Bertacco, Eric E Fullerton, and Stefano Bonetti. Inertial spin dynamics in epitaxial cobalt films. *Physical Review Letters*, 129(23):237201, 2022.
- Rodolfo Rodriguez, Mikhail Cherkasskii, Rundong Jiang, Ritwik Mondal, Arezoo Etesamirad, Allison Tossounian, Boris A Ivanov, and Igor Barsukov. Spin inertia and auto-oscillations in ferromagnets. *Physical Review Letters*, 132(24):246701, 2024.
- S Jain, V Novosad, FY Fradin, JE Pearson, V Tiberkevich, AN Slavin, and SD Bader. From chaos to selective ordering of vortex cores in interacting mesomagnets. *Nature communications*, 3(1):1330, 2012.
- A Pivano and VO Dolocan. Chaotic dynamics of magnetic domain walls in nanowires. *Physical Review B*, 93(14):144410, 2016.
- Konstantin Y Guslienko, Rafael Hernández Heredero, and Oksana Chubykalo-Fesenko. Nonlinear gyrotropic vortex dynamics in ferromagnetic dots. *Physical Review B—Condensed Matter and Materials Physics*, 82(1):014402, 2010.

- Roman V Ovcharov, Mohammad Hamdi, Boris A Ivanov, Johan Åkerman, and Roman S Khymyn. Antiferromagnetic droplet soliton driven by spin current. *Applied Physics Letters*, 124(17), 2024.
- Massimiliano d’Aquino, Salvatore Perna, Matteo Pancaldi, Riccardo Hertel, Stefano Bonetti, and Claudio Serpico. Micromagnetic study of inertial spin waves in ferromagnetic nanodots. *Physical Review B*, 107(14):144412, 2023.
- Zukhra Gareeva and Konstantin Guslienko. Nutation excitations in the gyrotropic vortex dynamics in a circular magnetic nanodot. *Nanomaterials*, 13(3):461, 2023.
- Albert Fert, Nicolas Reyren, and Vincent Cros. Magnetic skyrmions: advances in physics and potential applications. *Nature Reviews Materials*, 2(7):1–15, 2017.
- S Jiang, S Chung, M Ahlberg, A Frisk, R Khymyn, Q Tuan Le, H Mazraati, A Houshang, O Heinonen, and J Åkerman. Magnetic droplet soliton pairs. *Nature Communications*, 15(1):2118, 2024.
- F Garcia-Sanchez, J Sampaio, N Reyren, V Cros, and JV Kim. A skyrmion-based spin-torque nano-oscillator. *New Journal of Physics*, 18(7):075011, 2016.
- WanJun Jiang, Gong Chen, Kai Liu, Jiadong Zang, Suzanne GE Te Velthuis, and Axel Hoffmann. Skyrmions in magnetic multilayers. *Physics Reports*, 704:1–49, 2017.
- Zi-Lan Deng, Tan Shi, Alex Krasnok, Xiangping Li, and Andrea Alù. Observation of localized magnetic plasmon skyrmions. *Nature Communications*, 13(1):8, 2022.
- Arnold Markovich Kosevich, BA Ivanov, and Alexander S Kovalev. Magnetic solitons. *Physics Reports*, 194(3-4): 117–238, 1990.
- Seyed Majid Mohseni, SR Sani, J Persson, TN Anh Nguyen, Sunjae Chung, Ye Pogoryelov, PK Muduli, E Iacocca, A Eklund, RK Dumas, et al. Spin torque-generated magnetic droplet solitons. *Science*, 339(6125):1295–1298, 2013.
- B Roessli, J Schefer, GA Petrakovskii, B Ouladdiaf, M Boehm, U Staub, A Vorotinov, and L Bezmaternikh. Formation of a magnetic soliton lattice in copper metaborate. *Physical review letters*, 86(9):1885, 2001.
- VM Rothos, IK Mylonas, and T Bountis. Dissipative soliton dynamics of the landau–lifshitz–gilbert equation. *Theoretical and Mathematical Physics*, 215(2):622–635, 2023.
- Marcel G. Clerc, Saliya Coulibaly, and David Laroze. Localized states beyond the asymptotic parametrically driven amplitude equation. *Phys. Rev. E*, 77:056209, May 2008. doi:10.1103/PhysRevE.77.056209. URL <https://link.aps.org/doi/10.1103/PhysRevE.77.056209>.
- Marcel G. Clerc, Saliya Coulibaly, and David Laroze. Nonvariational ising-bloch transition in parametrically driven systems. *International Journal of Bifurcation and Chaos*, 19(08):2717–2726, 2009b. doi:10.1142/S0218127409024438. URL <https://doi.org/10.1142/S0218127409024438>.
- Marcel G. Clerc, Saliya Coulibaly, and David Laroze. Localized states and non-variational ising–bloch transition of a parametrically driven easy-plane ferromagnetic wire. *Physica D: Nonlinear Phenomena*, 239(1):72–86, 2010b. ISSN 0167-2789. doi:<https://doi.org/10.1016/j.physd.2009.10.008>. URL <https://www.sciencedirect.com/science/article/pii/S0167278909003236>.
- D. Urzagasti, D. Laroze, M. G. Clerc, and H. Pleiner. Breather soliton solutions in a parametrically driven magnetic wire. *Europhysics Letters*, 104(4):40001, dec 2013. doi:10.1209/0295-5075/104/40001. URL <https://dx.doi.org/10.1209/0295-5075/104/40001>.
- Amikam Aharoni. *Introduction to the Theory of Ferromagnetism*. Oxford University Press, 2001. URL <https://global.oup.com/academic/product/introduction-to-the-theory-of-ferromagnetism>.
- David Laroze, Jean Bragard, Omar J. Suarez, and Harald Pleiner. Characterization of the chaotic magnetic particle dynamics. *IEEE Transactions on Magnetics*, 47(10):3032–3035, 2011. doi:10.1109/TMAG.2011.2158072.
- David Laroze, David Becerra-Alonso, Jason A. C. Gallas, and Harald Pleiner. Magnetization dynamics under a quasiperiodic magnetic field. *IEEE Transactions on Magnetics*, 48(11):3567–3570, 2012. doi:10.1109/TMAG.2012.2207378.
- Bertrand Kibler, Amin Chabchoub, and Heremba Bailung. *Peregrine Soliton and Breathers in Wave Physics: Achievements and Perspectives*. Frontiers Research Topics. Frontiers Media SA, 2022. ISBN 9782889741113. URL <https://books.google.es/books?id=c-SBEAAAQBAJ>.
- William H. Press, Saul A. Teukolsky, William T. Vetterling, and Brian P. Flannery. *Numerical Recipes in FORTRAN: The Art of Scientific Computing*. Cambridge University Press, United States, 1993. ISBN 0521437210.
- D. Urzagasti, A. Aramayo, and D. Laroze. Soliton–antisoliton interaction in a parametrically driven easy-plane magnetic wire. *Physics Letters A*, 378(35):2614–2618, 2014b. ISSN 0375-9601. doi:<https://doi.org/10.1016/j.physleta.2014.07.013>. URL <https://www.sciencedirect.com/science/article/pii/S0375960114006872>.

- Alan Wolf, Jack B. Swift, Harry L. Swinney, and John A. Vastano. Determining lyapunov exponents from a time series. *Physica D: Nonlinear Phenomena*, 16(3):285–317, 1985. ISSN 0167-2789. doi:[https://doi.org/10.1016/0167-2789\(85\)90011-9](https://doi.org/10.1016/0167-2789(85)90011-9). URL <https://www.sciencedirect.com/science/article/pii/0167278985900119>.
- Masaki Sano and Yasuji Sawada. Measurement of the lyapunov spectrum from a chaotic time series. *Physical review letters*, 55(10):1082, 1985.
- K Ramasubramanian and MS Sriram. A comparative study of computation of lyapunov spectra with different algorithms. *Physica D: Nonlinear Phenomena*, 139(1-2):72–86, 2000.
- Michael T Rosenstein, James J Collins, and Carlo J De Luca. A practical method for calculating largest lyapunov exponents from small data sets. *Physica D: Nonlinear Phenomena*, 65(1-2):117–134, 1993.
- Karlheinz Geist, Ulrich Parlitz, and Werner Lauterborn. Comparison of different methods for computing lyapunov exponents. *Progress of theoretical physics*, 83(5):875–893, 1990.
- NC Pati. Spiral organization of quasi-periodic shrimp-shaped domains in a discrete predator–prey system. *Chaos: An Interdisciplinary Journal of Nonlinear Science*, 34(8), 2024.
- AA Mazanik, AE Botha, IR Rahmonov, and Yu M Shukrinov. Hysteresis and chaos in anomalous josephson junctions without capacitance. *Physical Review Applied*, 22(1):014062, 2024.
- A Bazzani, M Giovannozzi, CE Montanari, and G Turchetti. Performance analysis of indicators of chaos for nonlinear dynamical systems. *Physical Review E*, 107(6):064209, 2023.
- Richard J Field, Joana G Freire, and Jason AC Gallas. Quint points lattice in a driven belousov–zhabotinsky reaction model. *Chaos: An Interdisciplinary Journal of Nonlinear Science*, 31(5), 2021.
- Yifan Zhao and Yongxiang Zhang. Multiple tori intermittency routes to strange nonchaotic attractors in a quasiperiodically-forced piecewise smooth system. *Nonlinear Dynamics*, 112(8):6329–6338, 2024.
- Alexandre R. Nieto, Euaggelos E. Zotos, Jesús M. Seoane, and Miguel A. F. Sanjuán. Measuring the transition between nonhyperbolic and hyperbolic regimes in open hamiltonian systems. *Nonlinear Dynamics*, 99(4):3029–3039, Mar 2020. ISSN 1573-269X. doi:[10.1007/s11071-019-05433-4](https://doi.org/10.1007/s11071-019-05433-4). URL <https://doi.org/10.1007/s11071-019-05433-4>.
- Juan D. Bernal, Jesús M. Seoane, Juan C. Vallejo, Liang Huang, and Miguel A. F. Sanjuán. Influence of the gravitational radius on asymptotic behavior of the relativistic sitnikov problem. *Phys. Rev. E*, 102:042204, Oct 2020. doi:[10.1103/PhysRevE.102.042204](https://doi.org/10.1103/PhysRevE.102.042204). URL <https://link.aps.org/doi/10.1103/PhysRevE.102.042204>.
- Alvar Daza, Alexandre Wagemakers, and Miguel A. F. Sanjuán. Unpredictability and basin entropy. *Europhysics Letters*, 141(4):43001, feb 2023. doi:[10.1209/0295-5075/acb5be](https://doi.org/10.1209/0295-5075/acb5be). URL <https://dx.doi.org/10.1209/0295-5075/acb5be>.
- XiaoJun Yin, LiYang Xu, and Liangui Yang. Evolution and interaction of soliton solutions of rossby waves in geophysical fluid mechanics. *Nonlinear Dynamics*, 111(13):12433–12445, 2023.